The Astrophysical Journal, 888:53 (9pp), 2020 January 10 https://doi.org/10.3847/1538-4357/ab5e86

Quasi-periodic Pulsations of Gamma-Ray Emissions from a Solar Flare on 2017 September 6

D. Li[1,2], D. Y. Kolotkov[3,4], V. M. Nakariakov[3,5], L. Lu[1], and Z. J. Ning[1]
[1] Key Laboratory of Dark Matter and Space Astronomy, Purple Mountain Observatory, CAS, Nanjing 210033, People's Republic of China; lidong@pmo.ac.cn.
[2] State Key Laboratory of Space Weather, Chinese Academy of Sciences, Beijing 100190, People's Republic of China
[3] Centre for Fusion, Space and Astrophysics, Department of Physics, University of Warwick, Coventry CV4 7AL, UK
[4] Institute of Solar-Terrestrial Physics, Lermontov St., 126a, Irkutsk 664033, Russia
[5] St. Petersburg Branch, Special Astrophysical Observatory, Russian Academy of Sciences, 196140, St. Petersburg, Russia
Received 2019 September 10; revised 2019 November 7; accepted 2019 December 2; published 2020 January 8

Abstract

We investigate quasi-periodic pulsations (QPPs) of high-energy nonthermal emissions from an X9.3 flare (SOL2017-Sep-06T11:53), the most powerful flare since the beginning of solar cycle 24. The QPPs are identified as a series of regular and repeating peaks in the light curves in the γ- and hard X-ray (HXR) channels recorded by the *Konus-Wind*, as well as the radio and microwave fluxes measured by the CALLISTO radio spectrograph during the impulsive phase. The periods are determined from the global wavelet and Fourier power spectra as 24–30 s in the HXR and microwave channels, which are associated with nonthermal electrons, and ~20 s in the γ-ray band related to nonthermal ions. Both nonthermal electrons and ions may be accelerated by repetitive magnetic reconnection during the impulsive phase. However, we could not rule out other mechanisms, such as magnetohydrodynamic oscillation in a sausage mode. The QPP detected in this study is useful for understanding the particle acceleration and dynamic process in solar flares and also bridging the gap between stellar and solar flares because the energy realm of the X9.3 solar flare is almost comparable to a typical stellar flare.

Unified Astronomy Thesaurus concepts: Solar X-ray emission (1536); Solar gamma-ray emission (1497); Solar oscillations (1515); Solar flares (1496); Solar radio emission (1522)

1. Introduction

Quasi-periodic pulsations (QPPs) are a common feature in flaring emissions on the Sun and Sun-like stars. They are frequently detected as regular periodic peaks in light curves of solar/stellar flares, based on the time-series analysis (e.g., Nakariakov & Melnikov 2009; Pugh et al. 2016; Van Doorsselaere et al. 2016; McLaughlin et al. 2018, and references therein). The flare-related QPPs can be observed in almost all of the electromagnetic wave bands: radio (Aschwanden et al. 1994; Kupriyanova et al. 2016; Nakariakov et al. 2018), Hα (e.g., Srivastava et al. 2008), Lα (e.g., Milligan et al. 2017), ultraviolet and extreme ultraviolet (UV and EUV; Nakariakov et al. 1999; Kumar et al. 2016; Li et al. 2016), soft/hard X-rays (SXR/HXR; Zimovets & Struminsky 2010; Tan et al. 2016; Hayes et al. 2019), and even γ-rays (Nakariakov et al. 2010). Furthermore, QPPs are studied in spectroscopic observations, such as the Doppler velocity, line intensity, and width of hot emission lines (e.g., Wang et al. 2002; Tian et al. 2016; Brosius & Inglis 2018). The characteristic periods of flare-related QPPs appear in a broad range, from subseconds through seconds to dozens of minutes (Karlický et al. 2005; Shen & Liu 2012; Inglis et al. 2016; Kolotkov et al. 2018). Often, QPPs show a similar period in a broad wavelength range (Dolla et al. 2012; Kumar et al. 2016; Ning 2017). On the other hand, QPPs in the same event can exhibit multiple periods in a single wave band (Chowdhury et al. 2015; Kolotkov et al. 2015; Li & Zhang 2017). In some cases, the period ratios are found to correspond to the period ratios typical for magnetohydrodynamic (MHD) modes, such as sausage modes (Inglis & Nakariakov 2009).

Up to now, the physical mechanism responsible for the generation of QPPs is still an open issue (see Van Doorsselaere et al. 2016 and McLaughlin et al. 2018 for reviews of various theoretical models). In particular, flare-related QPPs observed in nonthermal emissions (i.e., radio, microwave, HXR, and γ-rays) are associated with accelerated electrons or ions, which might be produced by a periodic energy release (Kliem et al. 2000; McLaughlin et al. 2018). The short-period QPPs detected in radio and microwave emissions may be related to the dynamic interaction between waves and energetic particles, while the long-period QPPs observed in white light and UV and EUV wave bands are usually thought to be associated with the dynamics of the emitting plasmas (Aschwanden 1987; Nakariakov et al. 2006; Nakariakov & Melnikov 2009). In particular, QPPs can be driven by periodically induced magnetic reconnection (e.g., by MHD oscillations), or may be modulated by MHD waves such as slow, kink, and sausage waves, or could be a signature of spontaneous repetitive magnetic reconnection (by a magnetic dripping mechanism). It is likely that different classes of QPPs are produced by different mechanisms (Nakariakov & Melnikov 2009; Van Doorsselaere et al. 2016; McLaughlin et al. 2018).

QPPs in the γ-ray band are rarely reported. To date, only a 40 s QPP was found in a γ-ray flux in an X1.7 flare (Nakariakov et al. 2010). In this study, we analyze the X9.3 flare on 2017 September 6, which was the most powerful flare since 2005. Its released energy could even be in the realm of a typical stellar flare (see Kolotkov et al. 2018). In this paper, we demonstrate the presence of QPPs in radio, microwave, HXR, and also γ-ray channels in this flare. Our observational results could be helpful for understanding the particle acceleration and dynamic process in most powerful solar/stellar flares (Nakariakov et al. 2010; McLaughlin et al. 2018).

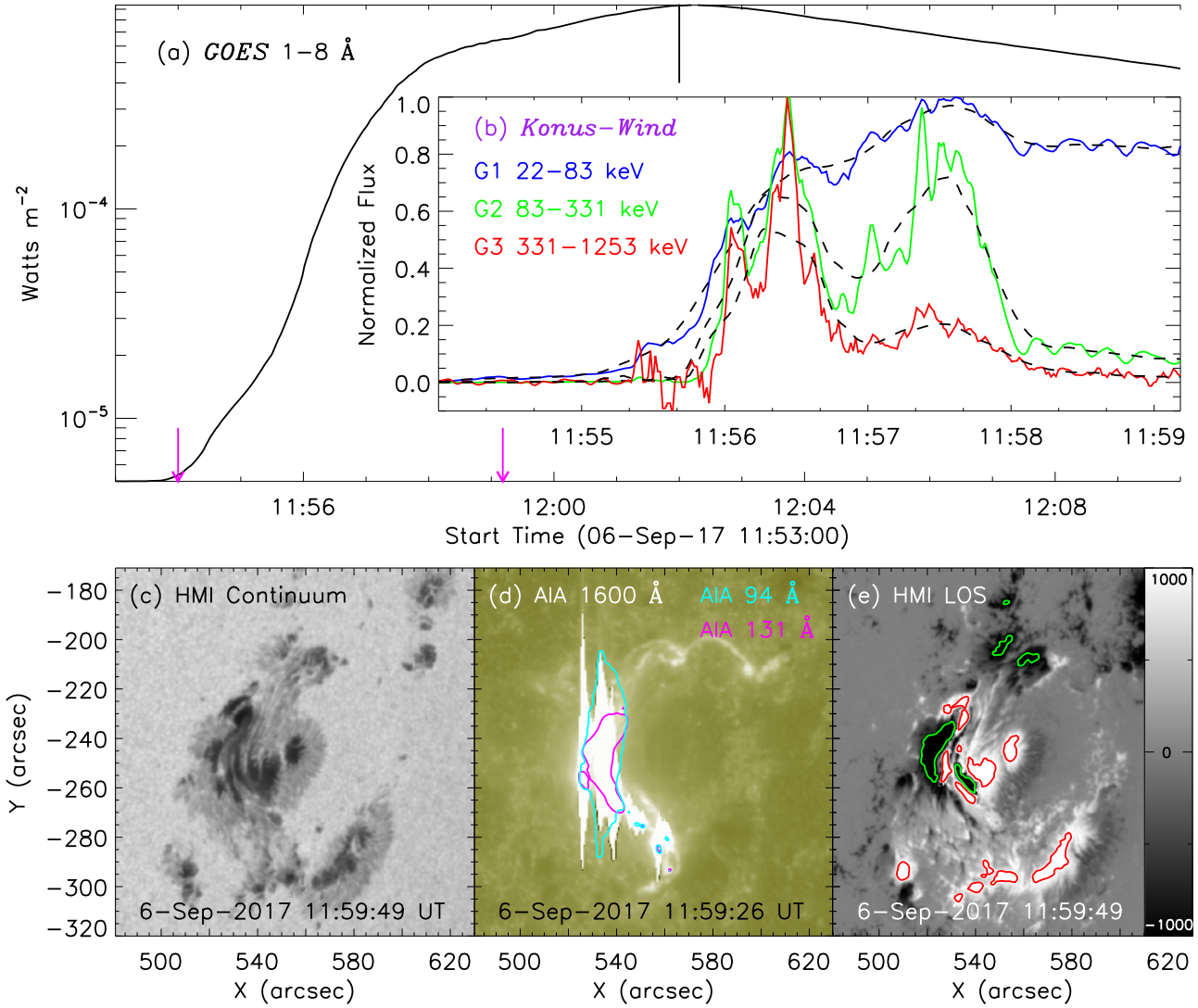

Figure 1. Panels (a) and (b): light curves in *GOES* 1–8 Å (black), *Konus-Wind* 22–83 keV (blue), 83–331 keV (green), and 331–1253 keV (red). The black dashed lines in panel (b) show the trended light curves. The short vertical line marks the flaring peak time, and two magenta arrows outline the time range in panel (b). Panel (c): HMI continuum filtergram. Panel (d): AIA 1600 Å image; the magenta and cyan contours are derived from AIA 131 Å and 94 Å images with levels of 20,000 DN s^{-1} and 3000 DN s^{-1}, respectively. Panel (e): HMI LOS magnetogram; the red and green contours represent the positive and negative magnetic fields at the level of ±1000 G.

2. Observations

On 2017 September 6, the most powerful flare (X9.3) of solar cycle 24 occurred in the active region of NOAA 12673. It started at ∼11:53 UT, peaked at around 12:02 UT, and ended at ∼12:10 UT in *GOES* SXR light curves at 1–8 Å, as shown by the black curve in Figure 1(a), where a short vertical line indicates the flaring peak time. The X9.3 flare was recorded by the *Konus-Wind* instrument during the impulsive phase in the HXR and γ-ray channels, such as G1 22–83 keV, G2 83–331 keV, and G3 331–1253 keV, as can be seen by the color lines in panel (b); here the time range is outlined by two magenta arrows in panel (a). *Konus-Wind* is a US–Russian experiment that aims to investigate solar flares and γ-ray bursts. It operates in two modes: the daily waiting mode, with an accumulation time of 2.944 s, and the triggered mode, with a nonuniform time cadence varying from 2 to 256 ms with a total duration of ∼250 s (Aptekar et al. 1995; Pal'shin et al. 2014). Note that the 3 s periodic dips with a duration of 30 ms in light curves are caused by instrumental effects due to the *Konus-Wind* occultation.[6] Therefore, the light curves measured from *Konus-Wind* are first interpolated to a uniform time cadence of 1.024 s, so the 3 s periodic dips are not apparent in Figure 1(b).

Figures 1(c)–(e) show the Helioseismic and Magnetic Imager (HMI) continuum filtergram, AIA 1600 Å image, and HMI line-of-sight (LOS) magnetogram with the same field of view of around 150″ × 150″, respectively. They have been preprocessed by "aia_prep.pro" and "hmi_prep.pro" in SolarSoftWare (Lemen et al. 2012; Schou et al. 2012). It can be seen that the powerful flare occurs in the active region that is apparently associated with a δ-type sunspot, as shown in panel (c). The X9.3 flare emits strong UV emission at the center region nearby ($x = 530''$, $y = -250''$), but it emits weak UV radiation at the north (such as $x = 580''$, $y = -200''$) and south ($x = 560''$, $y = -290''$) regions. The strong UV radiation is underlying a strong EUV emission observed in AIA 131 Å (magenta contours) and 94 Å (cyan contours) wavelengths, as

[6] http://www.ioffe.ru/LEA/kwsun/

shown in panel (d). The strong EUV emission could be attributed to hot flaring loops linking the apparent flare ribbons. On the other hand, the strong UV radiation is overlaying very complex and sheared magnetic polarity regions, which are composed of several strong positive and negative polarity sources, as indicated by the red and green contours in the center of panel (e). Based on the overall distribution of the positive and negative fields, the X9.3 flare is most likely a double-ribbon flare connected by hot flaring loops. The observed flare morphology is consistent with the standard "CSHKP" model (Carmichael 1964; Sturrock 1966; Hirayama 1974; Kopp & Pneuman 1976) or a 2D reconnection model (Sturrock & Coppi 1964). According to these models, the plasma at the reconnection region could be heated to more than 10 MK, and electrons will be efficiently accelerated to nonthermal energies. Subsequently, the released energy will be transported away from the reconnection site via nonthermal particles toward footpoints of the reconnection loop, and also outward along the open magnetic field. In this process, the flaring loop can be clearly seen in SXR or EUV wavelengths, with the HXR or microwave sources situated near the footpoints or loop top, and the flaring ribbons formed in the visible or UV wave band (e.g., Masuda et al. 1994; Lin et al. 2005; Fletcher et al. 2011; Benz 2017; Yan et al. 2018, and references therein). Moreover, the type III radio bursts are often accompanied by solar flares, which are thought to be the signatures of propagating beams of nonthermal electrons in the solar corona (e.g., Reid & Ratcliffe 2014). In our study, the flaring ribbons seem to be fragmented in the UV 1600 Å image, due to the image saturation of AIA observations during flare eruptions (see a discussion of this issue in Lemen et al. 2012).

The X9.3 flare was also measured by the ground-based CALLISTO radio spectrograph (Benz et al. 2009) located at GREENLAND (a) and BLEN5M (b), as shown in Figure 2. Panel (a) presents the radio dynamic spectrum at lower frequencies from ∼16.8 to ∼100.6 MHz, and the overplotted light curve is the radio flux at a frequency of around 60.8 MHz, as indicated by the short cyan line on the left-hand side. A series of transient bursts can be seen in the radio dynamic spectrum during the impulsive phase, between around 11:57 UT and 12:00 UT. They are characterized by a short time duration and a fast frequency drift; that is, they drift quickly from higher to lower frequencies over a short time. The observed behavior is consistent with typical type III radio bursts, which can be used to trace the propagating beams of flare-accelerated nonthermal electrons through the solar atmosphere (e.g., Wild & McCready 1950; Reid & Ratcliffe 2014). Meanwhile, much stronger bursts appear after the peak time of the flare, such as at ∼12:02 UT. The strong bursts exhibit a slow downward frequency drift, and the fundamental and harmonic frequencies are clearly seen in the radio dynamic spectrum. Thus, the slow drifts can be regarded as type II radio bursts, which are triggered by the electron beams accelerated by shock waves (e.g., Wild & McCready 1950; Mäkelä et al. 2018). However, because *Konus-Wind* measured the HXR and γ-ray emission in the flaring impulsive phase, before ∼12:00 UT, in this paper we analyze only the fast drifting radio bursts that could be directly compared with the HXR and γ-ray emission. Panel (b) gives the radio spectrogram at higher frequencies between ∼1040 and ∼1436 MHz, generally considered as microwave radiation. Similar to the radio dynamic spectrum at lower frequencies, the microwave spectrogram is also dominated by two pieces of strong emissions: one is characterized by a fast frequency drift between about 11:57 UT and 12:00 UT during the impulsive phase, and the other one exhibits a slow frequency drift after 12:00 UT. The overplotted light curve is the microwave flux at a frequency of near 1250.9 MHz. Both the radio and microwave fluxes at the frequencies of 60.8 and 1250.9 MHz are interpolated to a uniform time cadence of 1.0 s, which is close to that of the *Konus-Wind* light curves.

3. Data Analysis and Result

All the flaring fluxes during the impulsive phase recorded by *Konus-Wind* and CALLISTO appear to exhibit a signature of QPPs, that is, a series of regular and repeating pulsations with a period of roughly 30 s in the light curves, as can be seen in Figures 1(b) and 2(a). To study these flare-related QPPs in detail, we perform a wavelet analysis on the detrended light curves after removing a 30 s running average (e.g., Yuan et al. 2011; Tian et al. 2016; Li et al. 2018), as shown by the black dashed lines in Figures 1(b) and 2. The detrended light curves are used because we thereby enhance the shorter-period oscillations and suppress the long-period trend (see Kupriyanova et al. 2010, 2013; Gruber et al. 2011; Auchère et al. 2016 for the discussion and justification of this method). Here, the wavelet power is normalized in accordance with Parseval's theorem for wavelet analysis (see Torrence & Compo 1998), providing conservation of the total energy of the signal under the wavelet transform and thus allowing us to obtain a distribution of the spectral power across wavelet periods.

Figure 3(a) shows light curves that are detrended and normalized to the maximum fluxes measured by *Konus-Wind* in the HXR (G1 and G2) and γ-ray (G3) channels during the impulsive phase, that is, in the time interval ∼11:54:00–11:59:11 UT. They all appear to have periodic patterns, and the signals in the G1–G3 channels look approximately cophased. But the onset time in the G1 channel seems to be earlier than that in the G2 channel. Panels (b)–(d) present wavelet analysis results from the detrended light curves, all of which exhibit a coexistence of multiple periods: a long one about 70 s, a short one around 30 s, and a much shorter period near 10 s. The wavelet analysis spectra show that the onset time of QPPs in the G1 channel is earlier than in the G2 and G3 channels, and their duration times shorten with the emission energy from the HXR to γ-ray channels. From the confidence levels at 99.9% (see the large-region red contours that contain the bright region), we can see that the QPPs with a period of ∼30 s in the G1 channel start at around 11:55:16 UT and remain for roughly 120 s, while the similar QPPs in the G2 channel begin at about 11:55:37 UT and remain for around 110 s, and the QPPs in the G3 channel appear at near 11:55:33 UT and only last for about 75 s. Panels (e)–(g) present global wavelet results in three channels, which clearly show the presence of QPPs with a period of near 30 s. On the other hand, the spectral peak corresponding to the period of about 70 s is much lower than the confidence levels (red line), which could be attributed to the leakage of a slowly varying component of the background flaring trend, and this periodicity is not considered in this paper. Here, the dominant period is identified as the peak value in the global wavelet power spectrum, and its error bar is determined as the half FWHM of the peak global power (as performed by Li et al. 2018). Thus, the periods in the G1–G3 channels are estimated to be

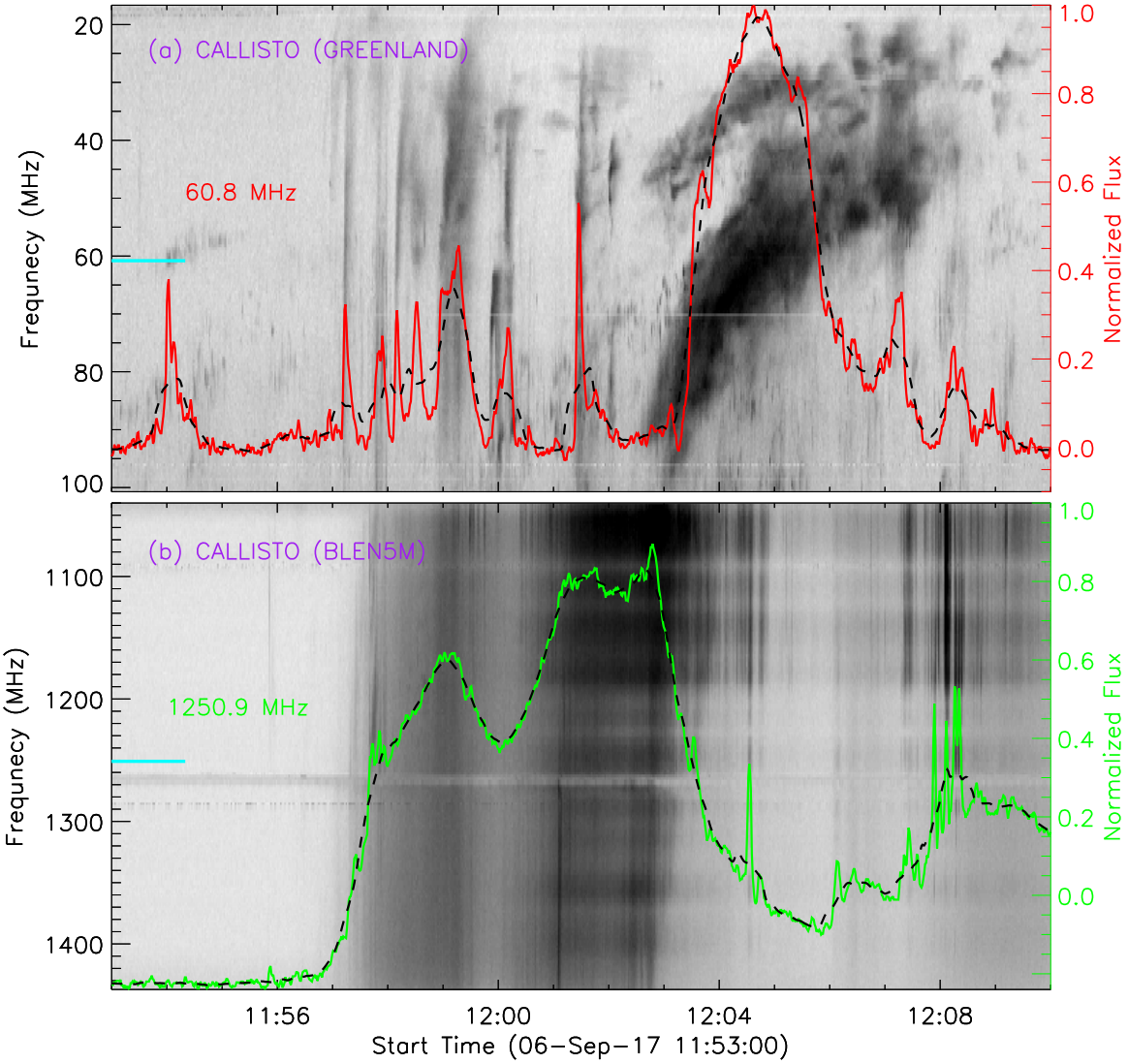

Figure 2. Radio dynamic spectra recorded by GREENLAND (a) and BLEN5M (b). The overplotted light curves are the radio/microwave fluxes indicated with a short cyan line on the left-hand side of each image, and the black dashed lines show their trended light curves.

$\sim$30 $\pm$ 6 s, $\sim$28 $\pm$ 8 s, and $\sim$20 $\pm$ 6 s, respectively. The estimated mean values of dominant periods seem to become shorter and shorter from HXR to γ-ray channels. However, they overlap within the estimated error bars. Finally, a much shorter period near 10 s (above the confidence levels) can be seen in the G1 and G2 channels, but it is below the confidence level in the G3 channel, as shown in panels (e)–(g). However, these ~10 s oscillations look rather sporadic and patchy, which may indicate in favor of their noisy origin (panels (b)–(d)), and their type of noise could be different from that considered in the wavelet analysis. Therefore, they are also disregarded in our study.

Figure 4 presents the same analysis results of radio emissions at low (60.8 MHz) and high (1250.9 MHz) frequencies between $\sim$11:56:00 UT and $\sim$11:59:59 UT. Panel (a) gives the normalized and detrended fluxes at the frequencies of 60.8 and 1250.9 MHz, which exhibit a number of regular and repeating peaks. Moreover, the peak times at these two frequencies are different, suggesting a frequency drift between them. Panels (b) and (c) display the wavelet power spectra, which show nearly the same onset time ($\sim$11:56:58 UT and $\sim$11:57:00 UT) of the QPPs but obviously different lifetimes ($\sim$130 and $\sim$85 s), as indicated by the confidence levels of 99.9% (red contours include the bright regions). Panels (d) and (e) show the global wavelet power spectra, from which we can see that only one peak is above the confidence level (red line) at the low and high frequencies, respectively. So the periods with error bars can be estimated to be $\sim$20 $\pm$ 6 s at the frequency of 60.8 MHz, and $\sim$24 $\pm$ 8 s at the frequency of 1250.9 MHz.

We further perform Fourier analysis of the original (but not detrended) light curves with the fast Fourier transform method (see Ning 2017), as shown in Figure 5. It can be seen that each Fourier power spectrum is dominated by a power law, which is usually identified as red noise in the astrophysical observations (Vaughan 2005). The red noise could be described by a power-law model, such as $P(f) \sim f^{\alpha}$. Here, f is the frequency, and α represents a negative slope. Meanwhile, a flat spectrum in the higher frequency region is often referred to as white noise. Such a superposition of red and white noise, dominating at lower and higher frequencies, respectively, is often observed in the solar atmosphere (e.g., Inglis et al. 2015; Kolotkov et al. 2016; Ning 2017). Figures 5(a) and (c) show that only one subpeak (magenta arrow) appears above the confidence levels (green lines) in the power-law spectra, confirming the presence

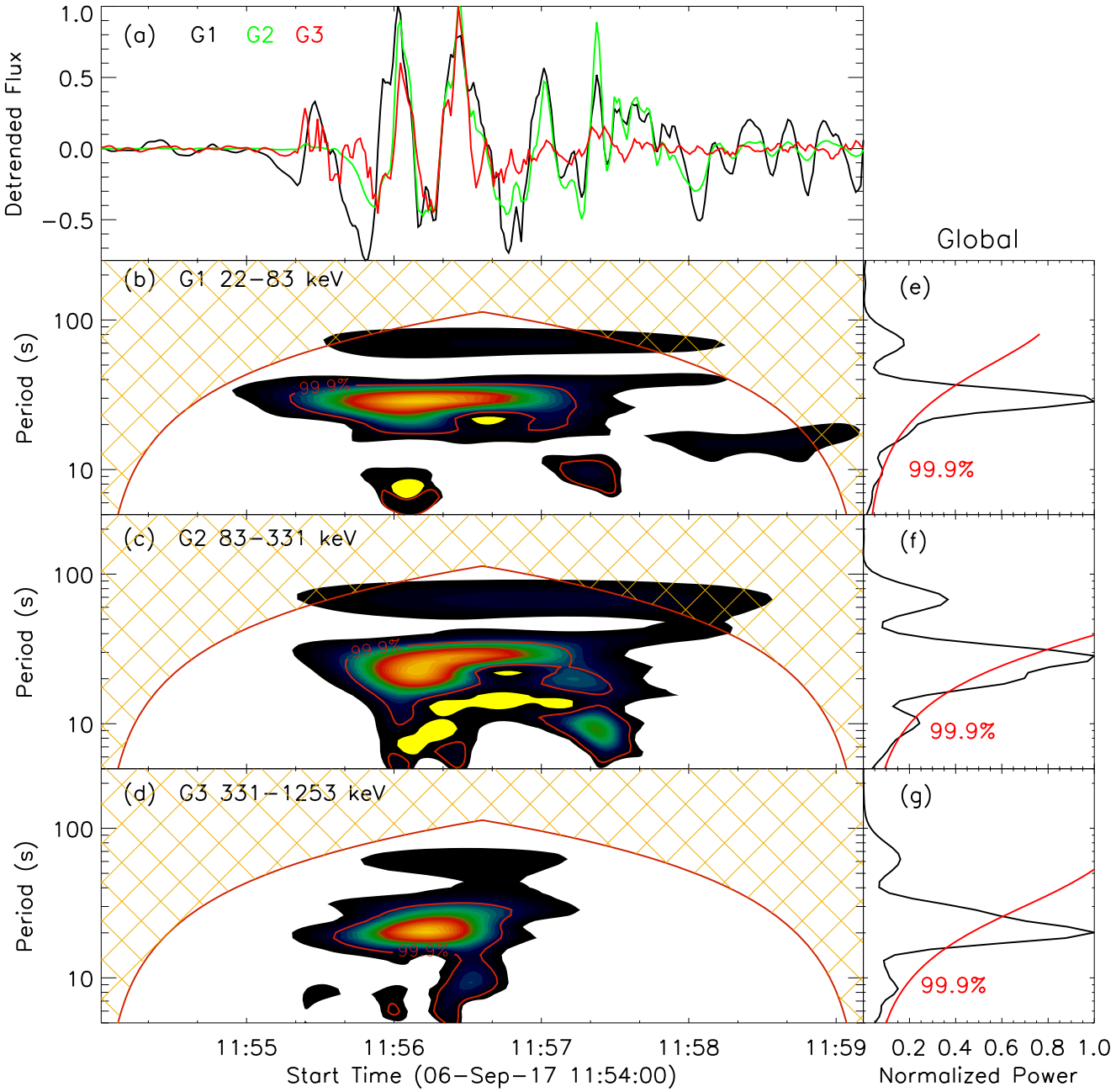

Figure 3. Panel (a): normalized and detrended light curves observed by *Konus-Wind* in HXR and γ-ray channels. Panels (b)–(d): their wavelet power spectra. Panels (e)–(g): their global wavelet power. The red lines indicate a significance level of 99.9%.

of shorter periods ($\sim$30 s and $\sim$20 s) in the two channels. On the other hand, there are two subpeaks (cyan and magenta arrows) above the confidence level in panel (b), suggesting the longer ($\sim$70 s) and shorter ($\sim$28 s) periods might be statistically significant in the G2 channel. According to Figure 1(b), the 70 s periodicity in the original light curves does not last for three complete oscillation cycles and could be attributed to the slow variations of the background flaring trends. As such, it might be a signature of localized transient activities, that is, episodic reconnection in the flare current sheet (e.g., Jelínek et al. 2017) or slow magnetoacoustic oscillations (e.g., Nakariakov et al. 2019). However, it is outside the scope of this study, since it only appears to be significant in the HXR (G2) channel, as shown in Figure 5(b), and is attributed to the long-period flare trend. We also notice that there are subpeaks (blue arrow) in flat spectra of all of the *Konus-Wind* light curves. They are not likely to represent real QPPs but could be caused by the 3 s periodic dips in the light curves that are due to the *Konus-Wind* occultation (Aptekar et al. 1995; Pal'shin et al. 2014). All of these Fourier power spectra do not show a subpeak near 10 s, further supporting that the 10 s period in Figure 3 is not real QPPs. Finally, panel (d) shows that only one subpeak (magenta arrow) is above the confidence level in the whole Fourier power spectrum, confirming the shorter period of $\sim$20 s in the radio frequency of 60.8 MHz.

4. Conclusion and Discussion

Using the multi-instrumental observations with *Konus-Wind* and the CALLISTO spectrographs (GREENLAND and

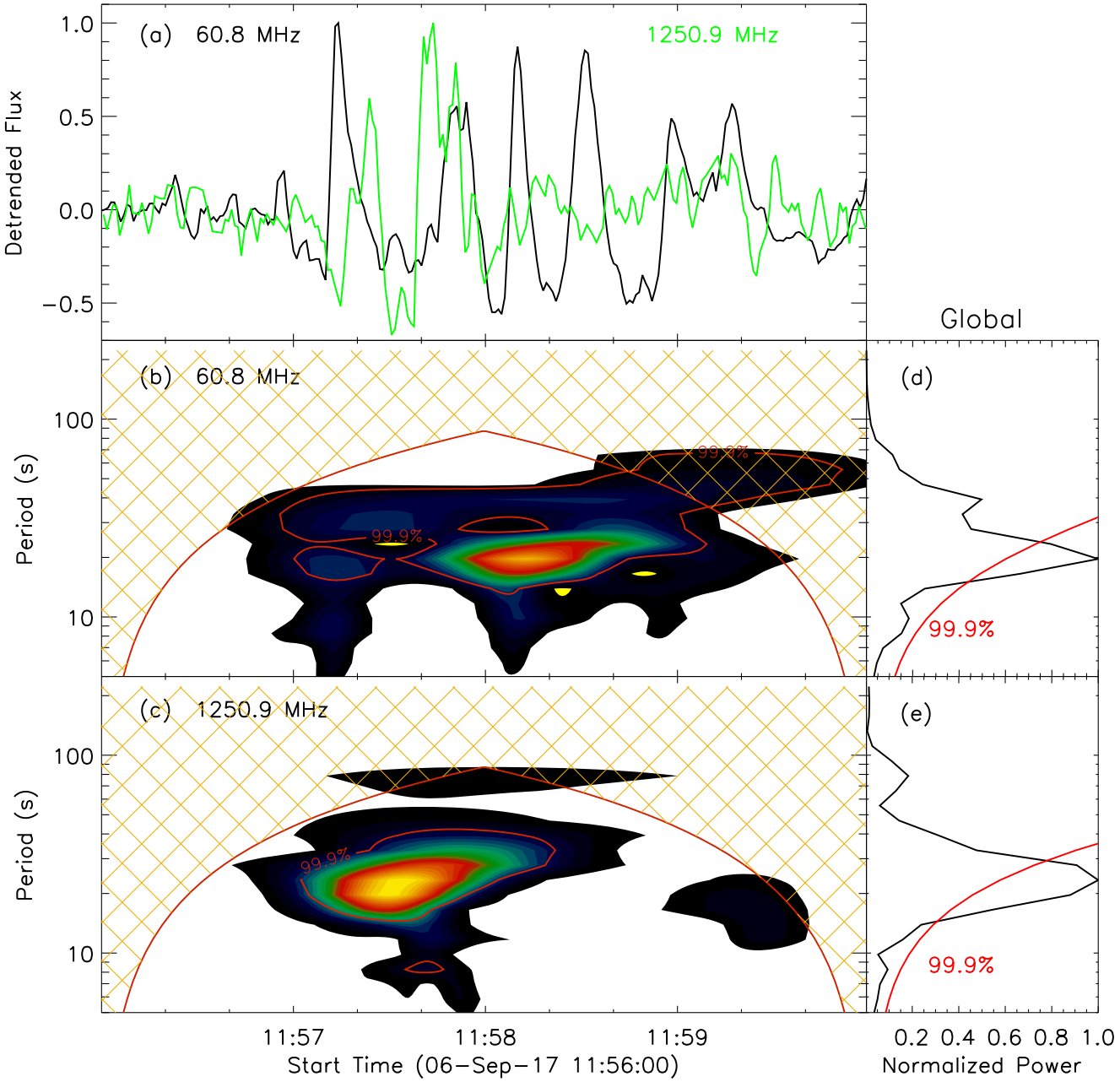

Figure 4. Panel (a): normalized and detrended light curves in radio and microwave bands. Panels (b) and (c): their wavelet power spectra. Panels (d) and (e): their global wavelet power. The red lines indicate a significance level of 99.9%.

BLEN5M), QPPs of high-energy nonthermal emissions are investigated in the X9.3 flare on 2017 September 6. Our primary results are summarized as follows:

1. QPPs are found in the HXR and γ-ray channels, and their periods are estimated as roughly 25 s, or more specifically, as $\sim 30 \pm 6$ s, $\sim 28 \pm 8$ s, and $\sim 20 \pm 6$ s in the energy channels of G1 22–83 keV, G2 83–331 keV, and G3 331–1253 keV, respectively. They are observed in the impulsive phase of the flare.
2. QPPs are also seen in radio and microwave emissions at both low and high frequencies, and their periods are estimated as $\sim 20 \pm 6$ s and $\sim 24 \pm 8$ s, which are consistent with the periods detected in the γ-ray and HXR wave bands, respectively. However, the QPPs detected in the radio band are delayed in comparison with the high-energy QPPs by $\sim$90 s, or about three cycles of the oscillation.
3. The QPPs observed in γ-ray emission are possibly associated with the accelerated ions, while the QPPs seen in the HXR and microwave emissions are most likely related to the accelerated electrons. Both the accelerated ions and electrons can be produced by a periodic regime of magnetic reconnection.

It is interesting that the 20 s QPPs are detected in the flaring γ-ray emission, which is thought to be related to nonthermal ions. Indeed, a high-energy part of the spectrum of this flare has been analyzed in detail by Lysenko et al. (2019), and they found a contribution from nuclear de-excitation lines, that is, the lines at 511 and 2223 keV, which confirms that the X9.3 flare does produce accelerated ions. On the other hand,

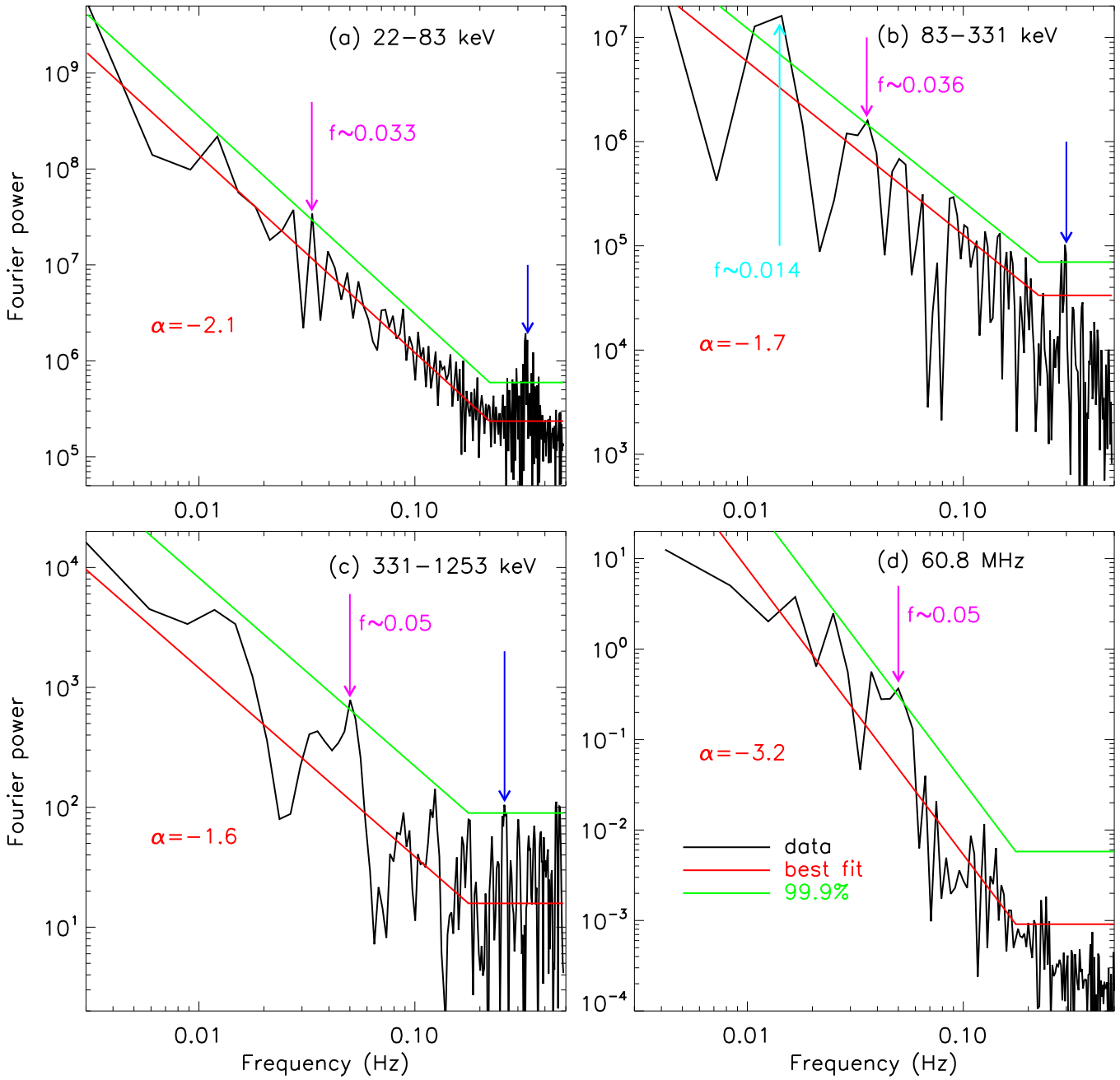

Figure 5. Fourier power spectra of the *Konus-Wind* light curves (a)–(c) and radio flux (d). The red line shows the best-fit result, and the green line represents the confidence level at 99.9%. The color arrows indicate the frequencies above the confidence level.

previous observations have shown that the flaring flux in the γ-ray band could have QPPs (Chupp 1983), and then the 40 s QPPs in the flaring γ-ray emission were studied in detail by Nakariakov et al. (2010). They concluded that the γ-ray QPPs were associated with accelerated ions produced by a magnetic reconnection that is periodically modulated by a global kink oscillation in a coronal loop situated nearby (Nakariakov et al. 2006). In this paper, the γ-ray QPPs are detected during the impulsive phase of an X9.3 flare and are most likely caused by nonthermal ions accelerated by magnetic reconnection too. The period of ~20 s might be triggered by the self-induced regimes of repetitive reconnection, or it could be caused by MHD oscillations (Nakariakov et al. 2006; Nakariakov & Melnikov 2009). However, it is impossible to determine the specific mechanism for the ~20 s periodicity because of the lack of the simultaneous imaging observations with the required time resolution, for example, shorter than several seconds.

It is worthwhile to stress that the QPPs detected in different wave bands have slightly different periods ranging from 20 to 30 s. The detected dominant periods shorten from HXR and microwave to γ-ray emissions, being 24–30 s in the HXR and microwave channels, but only 20 s in the γ-ray emission. Such a difference might be attributed to the different flare regions, which was first proposed by Nakariakov et al. (2010), who found that the HXR and γ-ray emissions came from two different sources. However, we cannot conclude that here, because of the absence of imaging observations in the microwave, HXR, and γ-ray channels. Conversely, the closest

periods are found in the HXR and microwave channels, which may be because their radiation sources are close to each other. On the other hand, taking into account the fact that the QPP periods detected in different wave bands coincide within the error bars, they might have the same value of about 25 s, and the slight difference could be ignored. More specifically, the observed similarity of the QPP patterns in the emission associated with the nonthermal electrons and ions indicates that either the acceleration or kinematics of those two species is modulated by the same quasi-periodic mechanisms. In the former case, the phenomenon of self-induced repetitive reconnection, that is, magnetic dripping, has been seen in numerical experiments (e.g., Liu et al. 2019; Thurgood et al. 2019). However, the relationship between the oscillation period and the parameters of the reconnecting plasma configuration for realistic values of transport coefficients, in particular the Lundquist number, needs to be established. The reconnection rate could also be modulated by an MHD oscillation (e.g., Nakariakov et al. 2006), while the efficiency of this mechanism has not been studied yet. Moreover, oscillatory motions of coronal plasma structures with a period of about 25 s could not be resolved with the available imaging telescopes. In the latter case, the kinematics of the charged particles could be affected by a periodic variation of the cross-sectional area of the magnetic flux tube filled in by those particles, by sausage oscillations, that is, by the Zaitsev–Stepanov mechanism (Zaitsev & Stepanov 1982). However, a comparative study of this effect on electrons and ions has not been performed yet, and, as mentioned above, the mother 25 s sausage oscillation could not be spatially resolved. Finally, to address these issues, we need more observations and cases, in particular, simultaneous imaging observations in the microwave, HXR, and γ-ray channels.

Based on the standard flare model (e.g., Sturrock & Coppi 1964; Masuda et al. 1994; Lin et al. 2005), both nonthermal electrons and ions are produced by the magnetic reconnection during the impulsive phase of a solar flare, while the HXR and microwave emissions of a solar flare are attributed to nonthermal electrons, and the flaring γ-ray emission is associated with nonthermal ions. Thus, the QPPs in the γ-ray, HXR, and radio and microwave channels suggest a similar dynamical process during the impulsive phase of a solar flare: nonthermal electrons and ions are periodically accelerated by the magnetic energy released by, for example, repetitive magnetic reconnection (see, Kliem et al. 2000; Nakariakov & Melnikov 2009; Nakariakov et al. 2018, and references therein). Moreover, the cross-correlation coefficients between the QPP signals detected in the G1 and G2 channels and the G2 and G3 channels are found to be 0.81 and 0.76, respectively. For all three channels, the highest correlation occurs for the zero time lags between the QPP signals, indicating the cotemporal nature of the QPPs. However, it is difficult to measure the correlation of the high-energy QPP signals with the radio QPP signals, as the radio QPPs occur about 90 s later than the HXR and γ-ray QPPs. But both the high-energy and radio QPPs clearly show a similar oscillation period. On the other hand, the observed periods of 20–30 s in the QPPs are very common in solar flares, which are often explained as sausage oscillations at coronal or flaring loops (e.g., Inglis et al. 2016; Tian et al. 2016; McLaughlin et al. 2018). Then the slightly different periods can be attributed to the gradual variations of the physical parameters at the oscillation flaring loops, that is, the small variations of loop length or plasma density of flaring loops (Hayes et al. 2016; Tian et al. 2016; Kolotkov et al. 2018). However, we cannot conclude this, because it is hard to detect these small-scale variations, due to the lack of high-resolution imaging observations. We note that the AIA images are saturated during the powerful solar flare.

It is also necessary to stress that the time delay of QPPs can be found in HXR, γ-ray, and radio channels. The onset time of QPPs in the G1 channel of *Konus-Wind* is earlier ($\sim$20 s) than in the G2 and G3 channels. The time delay might occur because the X-ray radiation in the G1 channel contains some SXR emissions, since its energy band is a little low, such as 22–83 keV. This is also consistent with the fact that the flare itself appears in the higher-energy bands later than in the lowest-energy one, as shown in Figure 1(b), while the QPPs in the G2 (HXR) and G3 (γ-ray) channels appear nearly in the same time, further confirming that they are caused by the accelerated charged particles produced by the same process of magnetic reconnection. The lifetime of QPPs in γ-rays is shorter than that in HXRs, which might be because the ion is much heavier than the electron, making it need more energy to accelerate. Thus, the power becomes more localized in time in the intensity wavelet from X-rays to γ-rays, as shown in Figures 3(b)–(d). On the other hand, the lifetime of QPPs in microwave emissions is close to that in γ-rays, but shorter than that in HXRs, suggesting that it also needs a large amount of energy to sustain radiation. The onset time of QPPs in the radio and microwave bands is delayed by $\sim$2 s, but they appear much later than QPPs in the HXR (G2) and γ-ray (G3) bands, by nearly 90 s. The latter delay might be associated with the radiation process (such as a specific velocity distribution) produced from radio/microwave emissions requiring a longer time than that responsible for the radiation in HXR or γ-ray bands (see Nishizuka et al. 2015). An additional reason for the time delay might be the time lag between the reconnection and acceleration processes, but that is still under discussion (e.g., Warmuth et al. 2009).

Finally, we notice that QPPs in the X9.3 flare have already been reported by Kolotkov et al. (2018). Using the time derivatives of the light curves measured by *GOES* and *SDO*/ESP, they found the periods of QPPs would drift from 12 s to 25 s during the impulsive and decay phases. The QPPs were interpreted as sausage oscillations at flaring loops, but they could not rule out the other mechanisms, such as repetitive reconnection. Time derivatives of SXR fluxes of solar flares often closely match the HXR/microwave light curves, which is known as the "Neupert effect" (e.g., Neupert 1968; Kahler et al. 1970; Ning 2008). However, the QPPs detected in these wave bands in the analyzed flare are of different periods, drifting from $\sim$12 s to $\sim$25 s (see Kolotkov et al. 2018), and are rather stable at $\sim$28/24 s in our study, respectively, suggesting different QPP-generation mechanisms operating in those wave bands. The difference in the QPP periods by a factor of two may also suggest that the oscillatory signals are linked with each other by a square dependence; that is, the oscillatory signal detected by Kolotkov et al. (2018) is a square of the signal detected in this study. However, theoretical models predicting such a dependence are absent. Also, in our analysis, we did not find long periods such as 4–5 minutes detected in this flare (Kolotkov et al. 2018), because the effective duration of light curves recorded by *Konus-Wind* is too short to detect them. On the other hand, the X9.3 flare was also observed by

the Large-Yield RAdiometer on board the PROBA2, and their light curves showed a clear signature of QPPs, as can be seen in Figure 2 of Dominique et al. (2018). The QPPs during the impulsive phase described there are similar to ours, but they are not discussed by the authors.

The QPPs of nonthermal emissions such as γ-ray, HXR, radio, and microwave are detected in a powerful solar flare (X9.3), which is in an energy realm of the typical stellar flares (Kolotkov et al. 2018). So it is helpful to bridge the energy gap between the solar and stellar flares (Maehara et al. 2015; Pugh et al. 2016), and it is also interesting for investigating the flaring energy release and particle acceleration on the Sun and Sun-like stars (Nakariakov et al. 2010; McLaughlin et al. 2018).

We thank the anonymous referee for the inspiring and valuable comments. The authors acknowledge Dr. S. Anfinogentov for his inspiring discussion. We thank the teams of *Konus-Wind*, *GOES*, *SDO*, and CALLISTO (the Institute for Data Science, FHNW Brugg/Windisch, Switzerland) for their open data use policy. This work is supported by NSFC under grants 11973092, 11603077, 11573072, 11790300, 11790302, 11729301, 11873095, the Youth Fund of Jiangsu Nos. BK20161095 and BK20171108, as well as the Strategic Priority Research Program on Space Science, CAS, grant Nos. XDA15052200 and XDA15320301. D.L. is supported by the Specialized Research Fund for State Key Laboratories. V.M.N. and D.Y.K. acknowledge support by the STFC consolidated grant ST/P000320/1. V.M.N. acknowledges the Russian Foundation for Basic Research grant No. 17-52-80064 BRICS-A. V.M.N. is also supported by the strategic development of science and technology grant No. G20190232001 of the State Administration of Foreign Experts Affairs of the Ministry of Science and Technology. The authors also acknowledge support from the ISSI-BJ team "Pulsations in Solar Flares: Matching Observations and Models." The Laboratory No. 2010DP173032.

ORCID iDs

D. Li https://orcid.org/0000-0002-4538-9350
D. Y. Kolotkov https://orcid.org/0000-0002-0687-6172
V. M. Nakariakov https://orcid.org/0000-0001-6423-8286

References

Aptekar, R. L., Frederiks, D. D., Golenetskii, S. V., et al. 1995, SSRv, 71, 265
Aschwanden, M. J. 1987, SoPh, 111, 113
Aschwanden, M. J., Benz, A. O., Dennis, B. R., et al. 1994, ApJS, 90, 631
Auchère, F., Froment, C., Bocchialini, K., et al. 2016, ApJ, 825, 110
Benz, A. O. 2017, LRSP, 14, 2
Benz, A. O., Monstein, C., Meyer, H., et al. 2009, EM&P, 104, 277
Brosius, J. W., & Inglis, A. R. 2018, ApJ, 867, 85
Carmichael, H. 1964, NASSP, 50, 451
Chowdhury, P., Srivastava, A. K., Dwivedi, B. N., et al. 2015, AdSpR, 56, 2769
Chupp, E. L. 1983, SoPh, 86, 383
Dolla, L., Marqué, C., Seaton, D. B., et al. 2012, ApJL, 749, L16
Dominique, M., Zhukov, A. N., Heinzel, P., et al. 2018, ApJL, 867, L24
Fletcher, L., Dennis, B. R., Hudson, H. S., et al. 2011, SSRv, 159, 19
Gruber, D., Lachowicz, P., Bissaldi, E., et al. 2011, A&A, 533, A61
Hayes, L. A., Gallagher, P. T., Dennis, B. R., et al. 2016, ApJL, 827, L30
Hayes, L. A., Gallagher, P. T., Dennis, B. R., et al. 2019, ApJ, 875, 33
Hirayama, T. 1974, SoPh, 34, 323
Inglis, A. R., Ireland, J., Dennis, B. R., et al. 2016, ApJ, 833, 284
Inglis, A. R., Ireland, J., & Dominique, M. 2015, ApJ, 798, 108
Inglis, A. R., & Nakariakov, V. M. 2009, A&A, 493, 259
Jelínek, P., Karlický, M., Van Doorsselaere, T., et al. 2017, ApJ, 847, 98
Kahler, S. W., Meekins, J. F., Kreplin, R. W., et al. 1970, ApJ, 162, 293
Karlický, M., Bárta, M., Mészárosová, H., et al. 2005, A&A, 432, 705
Kliem, B., Karlický, M., & Benz, A. O. 2000, A&A, 360, 715
Kolotkov, D. Y., Anfinogentov, S. A., & Nakariakov, V. M. 2016, A&A, 592, A153
Kolotkov, D. Y., Nakariakov, V. M., Kupriyanova, E. G., et al. 2015, A&A, 574, A53
Kolotkov, D. Y., Pugh, C. E., Broomhall, A.-M., et al. 2018, ApJL, 858, L3
Kopp, R. A., & Pneuman, G. W. 1976, SoPh, 50, 85
Kumar, P., Nakariakov, V. M., & Cho, K.-S. 2016, ApJ, 822, 7
Kupriyanova, E. G., Kashapova, L. K., Reid, H. A. S., et al. 2016, SoPh, 291, 3427
Kupriyanova, E. G., Melnikov, V. F., Nakariakov, V. M., et al. 2010, SoPh, 267, 329
Kupriyanova, E. G., Melnikov, V. F., & Shibasaki, K. 2013, SoPh, 284, 559
Lemen, J. R., Title, A. M., Akin, D. J., et al. 2012, SoPh, 275, 17
Li, D., Yuan, D., Su, Y. N., et al. 2018, A&A, 617, A86
Li, D., & Zhang, Q. M. 2017, MNRAS, 471, L6
Li, L. P., Zhang, J., Su, J. T., et al. 2016, ApJL, 829, L33
Lin, J., Ko, Y.-K., Sui, L., et al. 2005, ApJ, 622, 1251
Liu, C., Feng, X., Wan, M., et al. 2019, Ap&SS, 364, 127
Lysenko, A. L., Anfinogentov, S. A., Svinkin, D. S., et al. 2019, ApJ, 877, 145
Maehara, H., Shibayama, T., Notsu, Y., et al. 2015, EP&S, 67, 59
Mäkelä, P., Gopalswamy, N., & Akiyama, S. 2018, ApJ, 867, 40
Masuda, S., Kosugi, T., Hara, H., Tsuneta, S., & Ogawara, Y. 1994, Natur, 371, 495
McLaughlin, J. A., Nakariakov, V. M., Dominique, M., et al. 2018, SSRv, 214, 45
Milligan, R. O., Fleck, B., Ireland, J., et al. 2017, ApJL, 848, L8
Nakariakov, V. M., Anfinogentov, S., Storozhenko, A. A., et al. 2018, ApJ, 859, 154
Nakariakov, V. M., Foullon, C., Myagkova, I. N., et al. 2010, ApJL, 708, L47
Nakariakov, V. M., Foullon, C., Verwichte, E., et al. 2006, A&A, 452, 343
Nakariakov, V. M., Kosak, M. K., Kolotkov, D. Y., et al. 2019, ApJL, 874, L1
Nakariakov, V. M., & Melnikov, V. F. 2009, SSRv, 149, 119
Nakariakov, V. M., Ofman, L., Deluca, E. E., et al. 1999, Sci, 285, 862
Neupert, W. M. 1968, ApJL, 153, L59
Ning, Z. 2008, SoPh, 248, 99
Ning, Z. 2017, SoPh, 292, 11
Nishizuka, N., Karlický, M., Janvier, M., et al. 2015, ApJ, 799, 126
Pal'shin, V. D., Charikov, Y. E., Aptekar, R. L., et al. 2014, Ge&Ae, 54, 943
Pugh, C. E., Armstrong, D. J., Nakariakov, V. M., et al. 2016, MNRAS, 459, 3659
Reid, H. A. S., & Ratcliffe, H. 2014, RAA, 14, 773
Schou, J., Borrero, J. M., Norton, A. A., et al. 2012, SoPh, 275, 327
Shen, Y., & Liu, Y. 2012, ApJ, 753, 53
Srivastava, A. K., Zaqarashvili, T. V., Uddin, W., et al. 2008, MNRAS, 388, 1899
Sturrock, P. A. 1966, Natur, 211, 695
Sturrock, P. A., & Coppi, B. 1964, Natur, 204, 61
Tan, B., Yu, Z., Huang, J., et al. 2016, ApJ, 833, 206
Thurgood, J. O., Pontin, D. I., & McLaughlin, J. A. 2019, A&A, 621, A106
Tian, H., Young, P. R., Reeves, K. K., et al. 2016, ApJL, 823, L16
Torrence, C., & Compo, G. P. 1998, BAMS, 79, 61
Van Doorsselaere, T., Kupriyanova, E. G., & Yuan, D. 2016, SoPh, 291, 3143
Vaughan, S. 2005, A&A, 431, 391
Wang, T., Solanki, S. K., Curdt, W., et al. 2002, ApJL, 574, L101
Warmuth, A., Mann, G., & Aurass, H. 2009, A&A, 494, 677
Wild, J. P., & McCready, L. L. 1950, AuSRA, 3, 387
Yan, X. L., Yang, L. H., Xue, Z. K., et al. 2018, ApJL, 853, L18
Yuan, D., Nakariakov, V. M., Chorley, N., et al. 2011, A&A, 533, A116
Zaitsev, V. V., & Stepanov, A. V. 1982, SvAL, 8, 132
Zimovets, I. V., & Struminsky, A. B. 2010, SoPh, 263, 163